Nanoscale Advances

ROYAL SOCIETY OF CHEMISTRY

PAPER

View Article Online
View Journal | View Issue

Cite this: *Nanoscale Adv.*, 2021, **3**, 2325

Near-infrared light excited photodynamic anticancer therapy based on UCNP@AIEgen nanocomposite†

Shihui Ding,‡[a] Wenbo Wu,‡[bf] Tingting Peng,‡[c] Wen Pang,[a] Pengfei Jiang,[a] Qiuqiang Zhan,[c] Shuhong Qi,[de] Xunbin Wei,*[agh] Bobo Gu*[a] and Bin Liu*[b]

Received 24th November 2020
Accepted 17th February 2021

DOI: 10.1039/d0na00985g

rsc.li/nanoscale-advances

Photodynamic therapy (PDT), a clinically approved cancer treatment strategy, features non-invasiveness, few side-effects, high spatial resolution, *etc.* The advancement of PDT has been significantly restricted by the penetration depth of the excitation light. Herein, an effective fluorogen, TBD, with aggregation-induced emission characteristics (AIEgen) and high reactive-oxygen-species (ROS) generation efficiency was reported and integrated with a near infrared (NIR) light excitable upconversion nanoparticle (UCNP) to construct NIR light excitable UCNP@TBD nanocomposites. The formed nanocomposite has excellent photostability, good biocompatibility, and efficient ROS generation under NIR light excitation *via* Förster resonance energy transfer (FRET), enabling NIR light excited PDT. Moreover, the proposed NIR light excited PDT can break the impasse between the penetration depth and excitation volume in conventional PDT, effectively improving the anticancer therapeutic outcome. *In vitro* cancer cell ablation and *in vivo* tumor growth inhibition validated that the proposed UCNP@TBD nanocomposite is a promising NIR light excitable PDT agent with great potential for future translational research.

1. Introduction

Photodynamic therapy (PDT), which offers various benefits including non-invasiveness, few side effects, and high spatial resolution is a clinically approved treatment for cancer.[1] Since its first approval for clinical use to treat bladder cancer in 1993, PDT has been clinically applied to treat various cancers,[2,3] such as head and neck cancer,[4] lung cancer,[5] and digestive system cancer.[6] In PDT, photosensitizers (PSs) are injected, accumulate in the disease site, and generate reactive oxygen species (ROS) when excited by light at their absorption wavelength to irreversibly destroy the diseased tissues.[7]

Currently, porphyrin derivatives, widely used PSs, suffer from aggregation when dissolved in aqueous media, resulting in weakened fluorescence and reduced ROS generation, *i.e.* aggregation-caused quenching (ACQ).[8] Therefore, the therapeutic outcome of porphyrin-derivative-based PDT is limited. Fluorogens with aggregation-induced emission (AIE) characteristics (AIEgens) have great potential to overcome the ACQ issue, as they are almost non-emissive in the molecular state but emit strong fluorescence in the aggregate state when intramolecular motion is restricted. AIEgens can generate ROS efficiently *via* their delicate molecular design, enabling high performance image-guided PDT.[9–12] Other candidates to overcome the ACQ issue include inorganic nanomaterials, such as graphene quantum dots (QDs), black phosphorus, and carbon dots.[13–17] Although all PSs mentioned above have good performance, *e.g.* graphene QDs possess an ultra-high ROS quantum yield of 1.3,[13] their absorption is usually located in the visible range. Visible light has limited penetration depth in biological tissue, significantly lowering the PDT efficiency.[18,19]

Considering that near infrared (NIR) light has much deeper penetration depth compared with visible light, NIR light excited PDT could expand its medical applications.[11] In recent years, various NIR light excited PSs have been designed and synthesized. Most of these NIR light excitable PSs have low-bandgap donor–acceptor (D–A) structures to facilitate both the

[a]*School of Biomedical Engineering, Shanghai Jiao Tong University, 1954 Huashan Road, Shanghai 200030, China. E-mail: bobogu@sjtu.edu.cn*

[b]*Department of Chemical and Biomolecular Engineering, National University of Singapore, 117585, Singapore. E-mail: cheliub@nus.edu.sg*

[c]*Centre for Optical and Electromagnetic Research, South China Academy of Advanced Optoelectronics, South China Normal University, Guangzhou 510006, China*

[d]*Britton Chance Center for Biomedical Photonics, Wuhan National Laboratory for Optoelectronics, Huazhong University of Science and Technology, Wuhan, Hubei 430074, China*

[e]*MoE Key Laboratory for Biomedical Photonics, Collaborative Innovation Center for Biomedical Engineering, School of Engineering Sciences, Huazhong University of Science and Technology, Wuhan, Hubei 430074, China*

[f]*Institute of Molecular Aggregation Science, Tianjin University, Tianjin 300072, China*

[g]*Biomedical Engineering Department, Peking University, Beijing 100081, China. E-mail: xwei@bjmu.edu.cn*

[h]*Key Laboratory of Carcinogenesis and Translational Research (Ministry of Education/Beijing), Peking University Cancer Hospital & Institute, Beijing, 100142, China*

† Electronic supplementary information (ESI) available. See DOI: 10.1039/d0na00985g

‡ These authors contributed equally.

photothermal and photosensitizing processes,[20,21] achieving improved anticancer therapeutic outcomes *via* synergistic PTT/PDT instead of PDT only. So far, several optical technologies have been proposed to excite PDT using NIR light. Two-photon PDT, which normally utilizes two NIR photons to excite PSs, could provide much better penetration depth; many PSs with larger two-photon absorption cross-sections *via* different two-photon absorption cross-section enhancement strategies[22] were designed and synthesized for two-photon PDT applications.[23–25] As a typical nonlinear optical phenomenon, two-photon PDT requires high power pumping and consequently can only excite the PSs within a highly focused spot, enabling precise three-dimensional manipulation.[26] However, the tiny excited domain limits two-photon PDT for cancer treatment. Other nonlinear optical phenomena, *e.g.* harmonic generation[27] and coherent anti-Stokes Raman scattering,[28] have also been used to improve PDT treatment depth, but they suffer from similar limitations as two-photon PDT. The upconversion process sequentially absorbs multiple low-energy photons to emit high-energy luminescence,[29,30] enabling the conversion from NIR light to visible light. It is possible to construct UCNP@PSs nanocomposites (UCNP: upconversion nanoparticle) to excite PSs using the upconverted fluorescence of NIR light excited UCNPs *via* Förster resonance energy transfer (FRET),[31,32] overcoming the penetration depth limitation. Moreover, UCNPs can be excited using a continuous-wave (CW) diode laser due to their high conversion efficiency.[33] This means that the upconversion process could efficiently eliminate the limitation of tiny excitation volume. Thus, various PSs including chlorin e6 (Ce6),[34] merocyanine 540 and zinc(II) phthalocyanine[35] were selected to construct UCNP@PS nanocomposites *via* covalent conjugation,[36] silica encapsulation[37] or self-assembly method.[38] Under NIR light excitation, UCNP@PS based PDT exhibited increased penetration depth and excitation volume, improving the treatment efficiency for tumors. However, the organic PSs used to construct the UCNP@PSs nanocomposites mentioned above suffered from ACQ, limiting the loading efficiency of PSs and consequently the therapeutic efficiency. In order to eliminate the loading efficiency limitation, AIEgens have also been used recently to construct UCNP@AIEgen for biomedical applications.[39–41] Due to its inherent AIE feature, a UCNP@AIEgen nanocomposite enables improved *in vitro* and *in vivo* photodynamic anticancer therapy and offers new biomedical applications, *e.g.* inducing and monitoring stem-cell differentiation.[40] It is worth noting that most of the UCNP@PS nanocomposites were excited by 980 nm light since the 980 nm light excitable UCNPs have many advantages, including a simple upconversion process, easy synthesis, *etc.*[42] However, the photothermal effect induced by a 980 nm laser is inevitable[43] and would interfere with the practical PDT evaluation even though it could enhance the anticancer therapy efficiency.[44,45] Moreover, the photothermal effect significantly lowers the penetration depth due to strong absorption.[43,46] In order to accurately evaluate the PDT effect and improve the penetration depth, the photothermal effect induced by light irradiation should be avoided.

Herein, core–shell UCNPs ($NaYF_4$:30% Yb^{3+}, 1% Tm^{3+}, 1% Nd^{3+}@$NaYF_4$:20% Nd^{3+}) were designed and synthesized, since Nd^{3+}-Yb^{3+} cascading sensitization is able to shift the traditional 980 nm excitation to around 800 nm, remarkably lowering photothermal interference and improving the penetration depth of excitation. We then engineered a new AIEgen PS (TBD) to match the Nd^{3+}-sensitized UCNPs emission peak and consequently constructed the UCNP@TBD nanocomposite *via* a modified nanoprecipitation method. The nanocomposite can be excited by an 808 nm CW laser, efficiently eliminating the issues of tiny excitation volume, penetration depth limitation and photothermal interference. TBD showed very effective ROS generation capability, making UCNP@TBD nanocomposite a promising NIR excitable PDT agent *via* FRET. Meanwhile, its good photostability and biocompatibility endow the nanocomposite with great potential for future translational research.

2. Materials and methods

2.1 Materials

The AIE PS of TBD was prepared as described in our previous work.[47] 1,2-Distearoyl-*sn*-glycero-3-phosphoethanolamine-*N*-[methoxy(polyethylene glycol)-2000]-Maleimide (DSPE-PEG-MAL) was purchased from Laysan. Cell Counting Kit-8 (CCK-8) was purchased from Dojindo. Calcein acetoxymethyl ester (calcein-AM) was purchased from Biolegend. 9,10-Anthracenediyl-bis(methylene)dimalonic acid (ABDA), tetrahydrofuran (THF), dimethyl sulfoxide (DMSO), propidium iodide (PI), yttrium(III) acetate hydrate (99.9%), ytterbium(III) acetate hydrate (99.9%), thulium(III) acetate hydrate (99.9%) and neodymium(III) acetate hydrate (99.9%) were purchased from Sigma-Aldrich. Sodium sulfate (98.0%), sodium hydroxide (NaOH, >98%), ammonium fluoride (NH_4F, >99.99%), 1-octadecene (90%) and oleic acid (90%) were purchased from Aladdin®, China. Methanol (reagent grade), ethanol (reagent grade), and cyclohexane (reagent grade) were purchased from Sinopharm Chemical Reagent Co., China. Cyclic arginine-glycine-aspartic acid (cRGD) was synthesized by GL Biochem (Shanghai) Ltd. Chlorin e6 (Ce6, ≥98%) was purchased from Cayman Chemical Company. RPMI medium, DMEM medium, and phosphate buffered saline (PBS, 1×) were purchased from HyClone. Fetal calf serum was purchased from ScienCell. All the reagents were used without further purification.

2.2 Synthesis of UCNPs

The co-doped $NaYF_4$:30% Yb^{3+}, 1% Tm^{3+}, 1% Nd^{3+}@$NaYF_4$:20% Nd^{3+} core–shell nanoparticles were synthesized using a previously reported co-precipitation strategy with modifications.[48] Briefly, 5 mL of $Ln(CH_3CO_2)_3$ (Ln = 1% Tm/68% Y/30% Yb/1% Nd) stock solution (0.2 M), 7.5 mL of oleic acid and 17.5 mL of 1-octadecene were mixed and heated to 150 °C with stirring for about 40 min, then cooled to room temperature. Subsequently, 2.5 mL of NH_4F (0.4 M) and 10 mL of sodium sulfate (1 M) were quickly added and mixed with the lanthanide-oleate precursor solution until uniform. Next, the reaction system was heated to 100 °C and kept at this temperature for 30 min under an argon

atmosphere, followed by incubation at 300 °C for 90 min. After precipitation, the core $NaYF_4$:30% Yb^{3+}, 1% Tm^{3+}, 1% Nd^{3+} was washed several times using ethanol and cyclohexane and preserved in 8 mL of cyclohexane for the subsequent synthesis of core–shell nanoparticles.

For the core–shell nanoparticle synthesis, 2 mL of $Y(CH_3COO_2)_3$ and 0.5 mL of $Nd(CH_3COO_2)_3$ stock solution (0.2 M) were added to a 50 mL flask, together with 3.75 mL of oleic acid and 8.75 mL of 1-octadecene. Similar to the procedure of core synthesis, the mixture was heated and kept at 150 °C under stirring for 40 min before it was cooled to room temperature. Then 4 mL of $NaYF_4$:30% Yb^{3+}, 1% Tm^{3+}, 1% Nd^{3+} was injected into the reaction flask as a growth template, followed by 1.25 mL of NH_4F (0.4 M) and 5 mL of sodium sulfate (1 M). The next steps were the same as in the synthesis of the core nanoparticles. Finally, the sample was re-dispersed in 4 mL fresh cyclohexane for use.

2.3 Preparation of UCNP@TBD nanocomposite

The UCNP@TBD nanocomposite was prepared *via* a modified nanoprecipitation method.[49] To transfer UCNPs from cyclohexane to THF, 1 mL of ethanol was added to 1 mL of UCNPs cyclohexane solution, then the supernatant was removed by centrifugation at 8000 rpm for 10 min. The precipitate was resuspended by adding 2 mL of THF. To synthesize UCNP@TBD, TBD (0.75 mg) and DSPE-PEG-MAL (5 mg) were dissolved in 2 mL of THF and mixed with the as-obtained UCNPs in THF (17.5 μL, 16 mg mL^{-1}), followed by sonication for 5 min. Then, the mixture was quickly injected into 18 mL of deionized water, immediately followed by sonication utilizing a probe sonicator (JY96-IIN, SCIENTZ) for 90 s to form UCNP@TBD nanocomposite. After THF was volatilized by stirring in a fume hood for 24 h, the solution was dialyzed with Milli-Q water for 48 h, during which the water was changed 6 times. Finally, the solution was stored at 4 °C for future use after filtration with a filter membrane (0.22 μm). The final concentration of synthesized UCNP@TBD nanocomposite was ~50 μg mL^{-1} based on TBD.

Preparation of cRGD-UCNP@TBD nanocomposite. The cRGD powder was added into UCNP@TBD aqueous solution according to the molar concentration ratio of DSPE-PEG-MAL to cRGD 1 : 3 and the solution was gently stirred for 12 h. After dialysis for 48 h and filtration with a 0.22 μm filter membrane to remove excess cRGD and larger nanoparticles, the cRGD-UCNP@TBD nanocomposite was stored at 4 °C for future use.

2.4 Loading efficiency of TBD on UCNP@TBD

The proportion of TBD loaded on the formed UCNP@TBD was determined by measuring the change in the characteristic absorption peak of TBD at 432 nm before and after removing the self-nucleated TBD by centrifugation. The loading efficiency was obtained by calculating the ratio of the mass of successfully loaded TBD to the mass of UCNP@TBD after removing impurities by dialysis and centrifugation.

2.5 ROS measurement

ABDA was selected as the ROS indicator and dissolved in DMSO (5 mM). After mixing the ABDA solution (20 μL) with UCNP@TBD aqueous solution (1980 μL, [nanocomposite] = 13 μg mL^{-1} based on TBD), the mixture solution was irradiated with a 200 mW cm^{-2} 808 nm laser (SR808NL-1W, LASEVER INC.) for different times and time-sequenced UV-Vis absorption spectra were recorded by spectrophotometer (UV1901PC, Shanghai AOYAN Scientific Instrument Co. LTD).

2.6 Cell culture

4T1 cells (mouse breast cancer cells) were cultured using advanced RPMI medium containing 10% fetal calf serum (FBS), 1% penicillin and streptomycin. HeLa cells (human cervix cancer cells) and U87 cells (human glioblastoma cells) were cultured in DMEM medium with the other conditions unchanged.

2.7 Cytotoxicity test

4T1 and HeLa cells were seeded in 96-well plates (5000 cells per well, 100 μL per well, respectively). To prevent the edge liquid from evaporating too quickly, PBS was added around the test wells. Once the cells adhered to the wall and the density was appropriate, various concentrations of UCNP@TBD or cRGD-UCNP@TBD nanocomposite were added and incubated for 24 h or 48 h. After being washed with fresh medium to remove the residual nanocomposite, the treated cells were incubated with CCK-8 dissolved in RPMI or DMEM medium. After 1.5 h of incubation, the absorption at 450 nm was measured by microplate reader (SpectraMax i3x, MOLECULAR DEVICES).

2.8 Cancer cell imaging

4T1 cells were selected for co-stain bioimaging studies. Once 4T1 cells were adhered to the walls of the confocal dishes, UCNP@TBD nanocomposite ([UCNP@TBD] = 50 μg mL^{-1} based on TBD) was added to stain for 3 h, 6 h, and 24 h. After being washed three times with PBS to remove the residual nanocomposite, 4T1 cells were treated with 4% paraformaldehyde (PFA) for 15 min and subsequently washed three times with PBS to remove excess PFA, followed by co-staining with DAPI (1 μg mL^{-1}) for 15 min. Finally, the nanocomposite and DAPI co-stained 4T1 cells were processed for bioimaging by confocal microscope (Leica SP8) after washing with PBS to remove the residual DAPI.

Three cancer cell lines, 4T1, HeLa, and U87, with different integrin expression levels were selected for bioimaging studies. When adhered to the wall of confocal dishes, the cells were incubated with UCNP@TBD or cRGD-UCNP@TBD nanocomposite ([nanocomposite] = 50 μg mL^{-1} based on TBD) for 6 h. After being washed three times with PBS to remove the residual nanocomposite, the nanocomposite stained cells were processed for bioimaging by confocal microscope (Leica SP8).

2.9 *In vitro* PDT

After incubation with UCNP@TBD nanocomposite ([nanocomposite] = 50 μg mL^{-1} based on TBD) for 24 h, the 4T1 cells were irradiated with NIR light (808 nm, 2.5 W cm^{-2}) for 40 min and subsequently incubated in fresh medium for 4 h, then incubated with calcein-AM (2 μM) and PI (2 μM) for 30 min for the cell viability assessment. The same PDT experiment was also performed in HeLa cells using cRGD-UCNP@TBD nanocomposite under the same conditions to study the targeting capability of the nanocomposite.

2.10 Animal models

All animal experiments were approved by the Bioethics Committee of the School of Biomedical Engineering, Shanghai Jiao Tong University, and were consistent with regulations for the care and use of experimental animals in China. Female BALB/c mice (5 weeks old) were purchased from Shanghai Laboratory Animal Center. 4T1 cells (1×10^6) were subcutaneously injected in the mammary fat pad of the underbelly of the mice to establish an *in situ* model of breast carcinoma. *In vivo* PDT experiments were performed once the tumor volume reached about 40 mm^3, as measured by vernier caliper and calculated by the formula (tumor volume= (diameter × $width^2$)/2).

2.11 *In vivo* PDT

The tumor-bearing mice were randomly divided into four groups. In the PDT group, mice were intratumorally injected with 50 μL of UCNP@TBD nanocomposite ([UCNP@TBD] = 10 mg kg^{-1} based on TBD). Three hours after injection of the nanocomposite, the mice were irradiated by NIR light (808 nm, 2.5 W cm^{-2}, 40 min) for treatment. During the PDT treatment, the temperature distribution around the tumor site was monitored by thermal imager (DT-980, CEM). In the PS and Laser groups, mice were only treated with UCNP@TBD nanocomposite ([UCNP@TBD] = 10 mg kg^{-1} based on TBD) or NIR light irradiation (808 nm, 2.5 W cm^{-2}, 40 min). In the Control group, the tumor-bearing mice received no treatment. Tumor size and mouse weight were measured every two days for two weeks after treatment.

2.12 Statistical analysis

Data presented in this research are shown as the average ± SD. The mean values of the tumor volumes from the PDT group were statistically compared to those of the other groups using the two-tailed paired Student's *t* test in GraphPad Prism 8 software.

3. Results and discussion

3.1 Preparation and characterization of UCNP@TBD nanocomposite

To construct the UCNP@AIEgen nanocomposite for NIR light excited PDT, the UCNPs and AIEgens were elaborately designed and synthesized, separately. It is well known that biological tissue has much stronger absorption of 980 nm light than of 808 nm light.[11] The 980 nm light irradiation would induce significant photothermal effects,[50] which would interfere with the PDT performance and lower the treatment depth.[46,51] Based on our previous studies,[52] Nd^{3+}-Yb^{3+} cascading sensitization is capable of shifting the traditional 980 nm excitation to the band around 800 nm. Thus, the core–shell UCNPs ($NaYF_4$:30% Yb^{3+}, 1% Tm^{3+}, 1% Nd^{3+}@$NaYF_4$:20% Nd^{3+}), with the energy level diagram shown in Fig. S1,† were synthesized as the energy donor. The synthesized UCNPs had an average size of 37 nm, measured by dynamic light scattering (DLS) as shown in Fig. S2A,† and exhibited three main emission peaks at 451 nm ($^1D_2$-$^3F_4$), 475 nm ($^1G_4$-$^3H_6$) and 650 nm ($^1G_4$-$^3F_4$) under 808 nm light irradiation, as shown in Fig. 1B. Compared with two-photon excitation which has tiny excitation volume, UCNPs can achieve much larger excitation volume under CW light excitation (Fig. S3†). In order to efficiently eliminate the ACQ issue and enable the Förster resonance energy transfer (FRET) effect in the nanocomposite for NIR light excited PDT application, a fluorogen with aggregation-induced emission characteristics (AIEgen), *i.e.* TBD (Fig. 1A), whose absorption appropriately covers the emission range of UCNPs, was designed and synthesized as the energy acceptor. As shown in Fig. 1B, TBD has a main absorption peak centered at 432 nm, which covers the emission of UCNPs. TBD shows bright emission centered at around 600 nm when adding water to its DMSO solution, but negligible emission in DMSO (Fig. 1C). To evaluate its performance, TBD was encapsulated with amphiphilic DSPE-PEG-MAL to form TBD dots with an average size of 30 nm as measured by DLS (Fig. S2B†). The fluorescence quantum yield (Φ) of the TBD dots is measured as 0.16. Subsequently, the ROS generation efficiency of TBD dots ([TBD dots] = 10 μM based on TBD) was studied. As shown in Fig. S4,† it could be calculated from the absorption changes of the ROS indicator ABDA (50 μM) in the presence of TBD dots that 82.5 nmol of ABDA was consumed under light irradiation for 1 min. The consumption rate of ABDA in the presence of TBD dots is higher than that in the presence of Ce6, indicating the good ROS generation ability of TBD dots.

Considering that the emission of UCNPs matches well with the absorption of TBD, as shown in Fig. 1B, the UCNPs and TBD were selected as the energy donor and acceptor, respectively. In order to enable efficient energy transfer from UCNPs to AIEgens, UCNP and TBD were encapsulated with amphiphilic DSPE-PEG-MAL to form UCNP-AIEgen nanocomposite, *i.e.* UCNP@TBD nanocomposite, by a modified nanoprecipitation method. The loading efficiency of TBD was measured as 14.8 wt%. Moreover, the synthesized UCNP@TBD showed good long-term stability in water and cell lysate, as shown in Fig. S5,† ensuring good performance in biomedical applications. The formed nanocomposite, with a particle size distribution measured by DLS and shown in Fig. S2C,† was also characterized by transmission electron microscope (TEM). Its inorganic core (UCNP) and organic shell size (TBD and DSPE-PEG-MAL) were measured to be 35 nm and 5.5 nm (Fig. S6A†), respectively. To further verify that the TBD molecules encapsulated the UCNP, ytterbium (Yb), phosphorus (P) and sulfur (S), which are

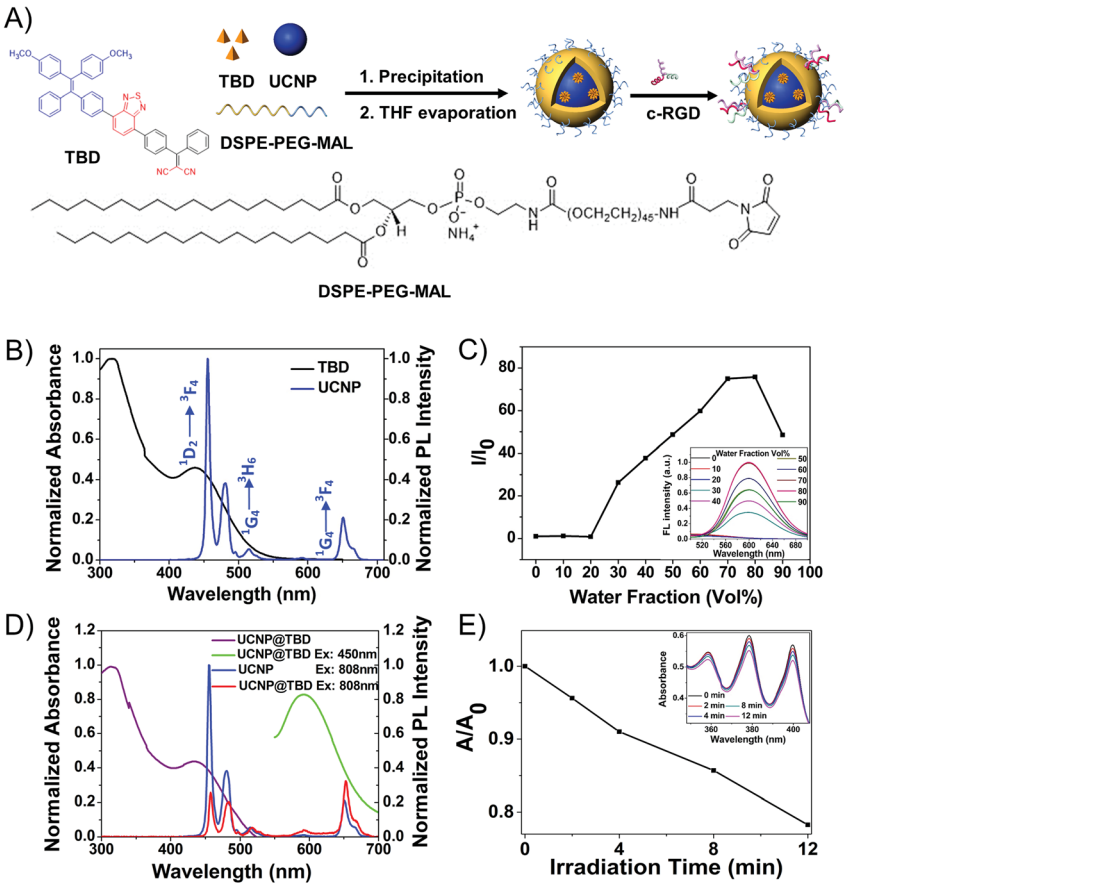

Fig. 1 (A) Synthesis of the UCNP@TBD nanocomposite. (B) Normalized UV-Vis absorption spectra of TBD dots ([TBD] = 13 μg mL^{-1}) and PL spectra of UCNPs (Ex: 808 nm, 12.5 mW, [UCNPs] = 16 mg mL^{-1}). (C) The changes in PL intensity of TBD in DMSO/water mixtures (Ex: 432 nm, [TBD] = 30 μg mL^{-1}) with different water fractions in the same total volume. The inset shows the PL spectra of TBD in different water fraction solvents. (D) Normalized UV-Vis absorption spectra of UCNP@TBD nanocomposite ([nanocomposite] = 13 μg mL^{-1} based on TBD) and normalized PL spectra of UCNPs (Ex: 808 nm, 12.5 mW, [UCNPs] = 16 mg mL^{-1}) and UCNP@TBD nanocomposite (Ex: 450 nm, 10 mW, [nanocomposite] = 13 μg mL^{-1} based on TBD; Ex: 808 nm, 12.5 mW, [nanocomposite] = 3.5 mg mL^{-1} based on UCNP). (E) The changing curve of the characteristic absorption peak (378 nm) of ABDA when the mixture solution of UCNP@TBD nanocomposite ([nanocomposite] = 13 μg mL^{-1} based on TBD) and ABDA (0.05 mM) was irradiated with NIR light (808 nm, 200 mW cm^{-2}) for different times. The measured UV-Vis absorption spectra are shown in the inset.

the characteristic elements of UCNP, DSPE-PEG-MAL and TBD, respectively, were selected to perform energy-dispersive spectrum (EDS) analysis. As shown in Fig. S6B,† all three elements display a spherical structure and the distribution diameters of P and S are obviously larger than that of Yb, meaning that DSPE-PEG-MAL effectively encapsulated TBD on the surface of UCNP. The formed nanocomposite ensures close proximity between UCNP and TBD, thereby enabling efficient activation of TBD to generate ROS by upconverted light from UCNP *via* FRET. Meanwhile, the spectra of the nanocomposite were also recorded to study the FRET effect between UCNP and TBD. As shown in Fig. 1D, the nanocomposite has similar absorption as TBD, indicating that TBD is successfully incorporated into the nanocomposite.

Compared with the emission of pure UCNP, the nanocomposite has weakened emission at 451 nm and 475 nm and similar emission at 650 nm when irradiated by 808 nm light. Moreover, an emission centered at 600 nm appeared, which matched well with the emission of TBD. These spectral responses of the nanocomposite confirmed that TBD could be excited by upconverted light from NIR light excited UCNP *via* FRET, enabling NIR light excited PDT.

3.2 Photostability and ROS generation capability of UCNP@TBD nanocomposite

Before characterizing its ROS generation capability, the photostability of the synthesized UCNP@TBD nanocomposite was studied. The absorption of the nanocomposite irradiated by NIR light (808 nm, 2.5 W cm^{-2}) was measured to investigate its photostability. As shown in Fig. S7A,† there were no significant changes in the absorption of the UCNP@TBD nanocomposite, while the absorption of Ce6 obviously decreased under irradiation (400–700 nm, ~60 mW cm^{-2}) for only 3 min (Fig. S7B†), which indicates much better photostability of the nanocomposite compared with that of Ce6. To characterize its ROS generation capability under NIR light irradiation, the nanocomposite ([UCNP@TBD] = 13 μg mL^{-1} based on TBD) was

mixed with the ROS indicator, *i.e.* ABDA (50 μM), and then irradiated with NIR light (808 nm, 200 mW cm^{-2}). Time-sequenced absorption spectra were measured as shown in Fig. 1E. With the increase of irradiation time, the characteristic absorption peak of ABDA in the presence of the nanocomposite obviously decreased, while the absorption of pure ABDA almost remained constant under the same irradiation, eliminating interference from ABDA decomposition by light irradiation (Fig. S7C†). These results indicate that the UCNP@TBD nanocomposite could generate ROS efficiently under NIR light irradiation.

3.3 Biocompatibility and *in vitro* PDT effect

The biocompatibility and cellular phototoxicity of the UCNP@TBD nanocomposite were evaluated. After incubation with the UCNP@TBD nanocomposite for different times, the cell viabilities of HeLa and 4T1 cells were evaluated with a standard CCK-8 assay. There was no significant difference between the cells treated with or without various concentrations of UCNP@TBD nanocomposite (10–50 μg mL^{-1}, based on TBD) for 24 and 48 h (Fig. S8†). To evaluate the cellular phototoxicity of NIR light, HeLa cells were irradiated with different power densities and subsequently stained with calcein-AM and propidium iodide (PI). As shown in Fig. S9,† even under NIR light irradiation for 40 min (808 nm, 2.5 W cm^{-2}), no change in calcein-AM intensity or the PI-positive, *i.e.* necrotic cells, was observed. These results indicate that the UCNP@TBD nanocomposite has excellent biocompatibility and NIR light irradiation has ultra-low cellular phototoxicity, enabling the UCNP@TBD nanocomposite to serve as a biocompatible PDT agent for anticancer applications.

It is well known that the lifetime (~200 ns) and diffusion range (~20 nm) of singlet oxygen are extremely limited,[53] so it is crucial that the photosensitizer is internalized by the cells for an effective therapeutic outcome. After staining 4T1 cells for 3 h, 6 h and 24 h, the fluorescence signal of the UCNP@TBD nanocomposite ([UCNP@TBD] = 50 μg mL^{-1} based on TBD) was clearly observed in the cytoplasm and was further enhanced with the increment of incubation time (Fig. S10†). Meanwhile, the measured spectra matched that of TBD, indicating that TBD was successfully encapsulated to form UCNP@TBD nanocomposite.

To further improve the internalization capability of the UCNP@TBD nanocomposite, especially for some specific cancer cells, the cRGD molecule was functionalized on the surface of the nanocomposite to form cRGD-UCNP@TBD nanocomposite. The zeta potentials and absorption spectra of UCNP@TBD and cRGD-UCNP@TBD were measured. After functionalization with cRGD, the zeta potential of the nanocomposite changed from −13 mV to −5 mV. Meanwhile, as shown in Fig. S11,† cRGD-UCNP@TBD had enhanced absorption at 200 nm and 320 nm, which are the characteristic absorptions of cRGD, as compared with UCNP@TBD. The changes in zeta potential and absorption spectra indicated that cRGD was successfully functionalized on the surface of UCNP@TBD. The biocompatibility of cRGD-UCNP@TBD nanocomposite was also characterized with a standard CCK-8 assay, shown in Fig. S8,† and there was no significant difference. Considering that cRGD can efficiently and specifically bind to integrin $\alpha_v\beta_3$, which is highly expressed in some cancer cells such as 4T1, HeLa, and U87, cRGD-UCNP@TBD and UCNP@TBD nanocomposites ([nanocomposites] = 50 μg mL^{-1} based on TBD) were incubated with different cancer cell lines, including HeLa, U87 and 4T1, for 6 h for comparation. The fluorescence signal of the nanocomposite was observed in the cytoplasm of all cell lines and the fluorescence intensity of UCNP@TBD nanocomposite in the cytoplasm of 4T1 cells was higher than those in HeLa and U87 cells. It was observed that the fluorescence intensity of cRGD-UCNP@TBD nanocomposite in the cytoplasm of all these cancer cells was enhanced (Fig. S12†). The inherent and enhanced internalization capability endows the nanocomposite with the potential to achieve an effective therapeutic outcome.

Considering its good ROS generation and internalization capability, UCNP@TBD is expected to efficiently generate intracellular ROS. 2′,7′-Dichlorofluorescin-diacetate (DCFH-DA), which oxidizes in the presence of ROS to emit the strong fluorescence signal of dichlorofluorescein (DCF), was selected as the ROS indicator to study the intracellular ROS generation capability of UCNP@TBD. After incubating either with both UCNP@TBD and DCFH-DA or with DCFH-DA alone, the 4T1 cells were irradiated and imaged with a confocal laser scanning microscope. As shown in Fig. S13 in the ESI,† a strong fluorescent signal of DCF was observed in the 4T1 cells incubated with both UCNP@TBD and DCFH-DA after 30 s irradiation, indicating the fast and efficient intracellular ROS generation capability of UCNP@TBD. In contrast, no fluorescence signal was observed in the absence of UCNP@TBD. This control study eliminates the possibility of any laser induced interference to the obtained results.

To study the cellular response under NIR excited PDT action, 4T1 cells were incubated with the UCNP@TBD nanocomposite ([UCNP@TBD] = 50 μg mL^{-1} based on TBD) for 24 h. Subsequently, the treated cells were washed three times to remove the residual nanocomposite and irradiated with NIR light (808 nm, 2.5 W cm^{-2}) for 40 min. Following the irradiation, cell viability was analyzed by staining with calcein-AM and PI for 30 min. As shown in Fig. 2, all cells treated with both UCNP@TBD nanocomposite and laser irradiation, *i.e.* PDT groups, were either PI-positive or detached, indicating the effective therapeutic outcome of the UCNP@TBD nanocomposite based PDT. Meanwhile, almost all the cells in the Control group (without any treatment), PS group (treated with UCNP@TBD nanocomposite only), and Laser group (treated with light irradiation only) show the calcein-AM fluorescent signal, meaning that UCNP@TBD nanocomposite or light irradiation alone cannot ablate cancer cells. Considering that the cRGD-UCNP@TBD nanocomposite has better internalization capability, its PDT effect was also investigated. HeLa cells were incubated with the same concentration of cRGD-UCNP@TBD nanocomposite ([cRGD-UCNP@TBD] = 50 μg mL^{-1} based on TBD) but only for 6 h, and then were irradiated with same light dose. More

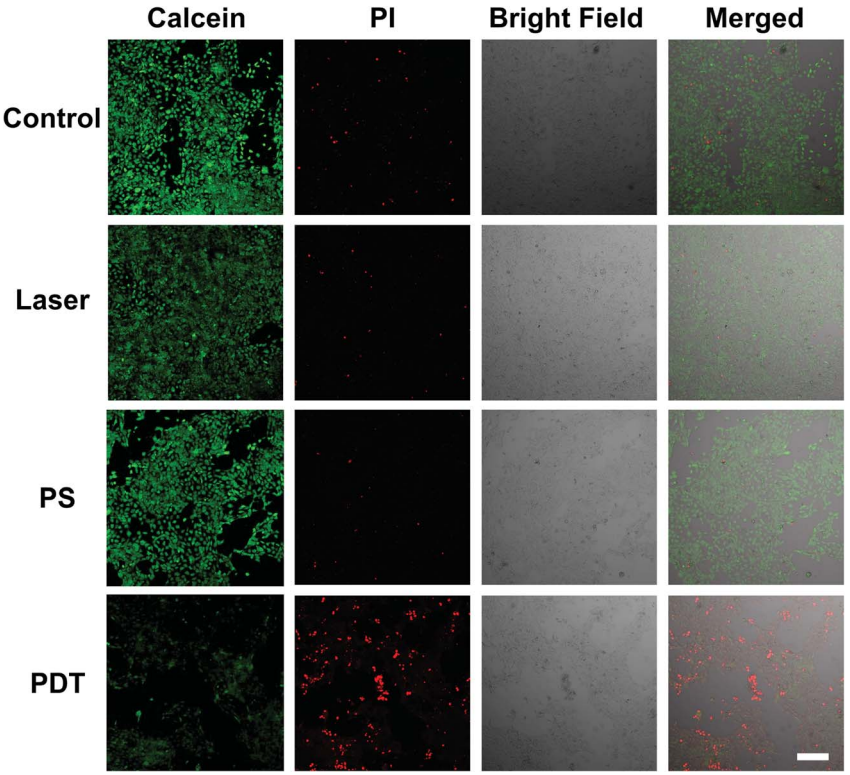

Fig. 2 Viability of 4T1 cells treated with/without UCNP@TBD followed by laser irradiation (Ex: 808 nm, 2.5 W cm^{-2}) for 40 min or treated with only UCNP@TBD or laser irradiation (Ex: 808 nm, 2.5 W cm^{-2}). [UCNP@TBD] = 50 μg mL^{-1} based on TBD, [calcein-AM] = 2 μM, [PI] = 2 μM, calcein-AM (Ex: 488 nm; Em: 505–525 nm) and propidium iodide (PI) (Ex: 552 nm; Em: 605–625 nm). Scale bar: 200 μm.

effective cancer cell ablation was obtained, as shown in Fig. S14.†

3.4 *In vivo* PDT effect of UCNP@TBD nanocomposite

Before performing the NIR light excited *in vivo* PDT studies, the penetration depth of the excited light was also investigated. As shown in Fig. S15,† the penetration depth of 808 nm light reached about 1.35 cm, enabling PDT to be performed at a significant depth. Considering its excitation volume (Fig. S3†) and penetration depth (Fig. S15†), the NIR light excited PDT based on UCNP@AIEgen nanocomposite could break the contradiction between penetration depth and excitation volume that exists in conventional PDT. Because the orthotopic tumor model is similar to the practical clinical pathogenesis model, the orthotopic breast tumor model was established by inoculating 4T1 cells in the abdominal mammary fat pad of mice. In the PDT group, UCNP@TBD nanocomposite (10 mg kg^{-1} based on TBD) was administrated *via* intratumoral injection. Three hours after injection, the tumor site was exposed to NIR light (808 nm, 2.5 W cm^{-2}) for 40 min with a 2 min interval every 20 min to further eliminate the photothermal effect. The temperature distribution at the tumor site was monitored by thermal imager during the treatment. As shown in Fig. S16,† the maximum temperature was 40.4 °C, which is less than the required temperature for photothermal treatment (PTT).[54] Thus, any interference from PTT could be eliminated. Meanwhile, mice in the control groups, including the control group (without any treatment), PS group (only treated with UCNP@TBD nanocomposite) and laser group (only treated with light irradiation), were monitored and compared. As shown in Fig. 3A, all the mice increased slightly in weight. Although the tumor sizes of mice from all groups increased, the tumor size increment rate of mice with PDT treatment was significantly

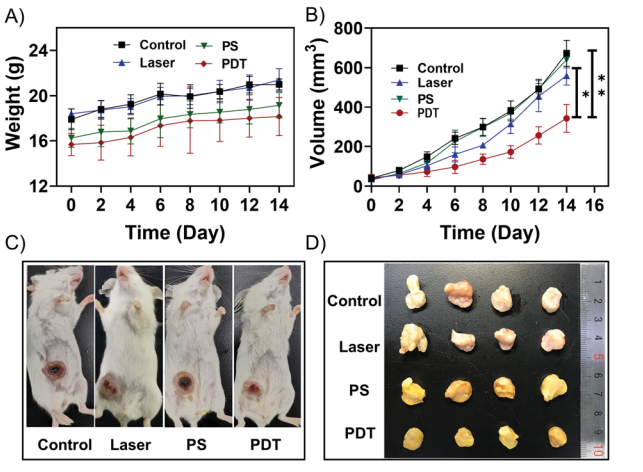

Fig. 3 (A) Animal weight of all groups measured for two weeks ($n = 4$). (B) Tumor volumes from different groups. (PDT *vs.* control, $^{**}p = 0.0073$; PDT *vs.* Laser, $^{*}p = 0.0229$; PDT *vs.* PS, $^{*}p = 0.0115$). (C) Representative photos of mice from control group, laser group, PS group and PDT group. (D) An image of the excised tumors.

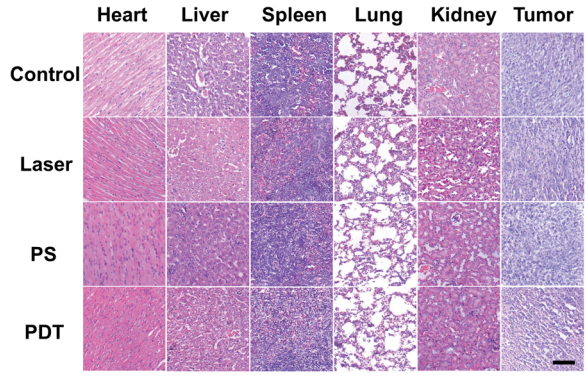

Fig. 4 H&E staining of main organs and tumors from different groups of mice. Scale bar: 50 μm.

lower than those of other mice, as shown in Fig. 3B, indicating that NIR excited PDT could efficiently inhibit tumor development. Representative photos of mice from different groups on day 14 are presented in Fig. 3C. Then, all the mice were sacrificed and the practical morphology of the tumors is shown in Fig. 3D. The tumors of PDT treated mice were significantly smaller than those of other groups, confirming the effectiveness of NIR excited PDT.

In addition, the tumor and main organs of the mice were harvested to observe histological changes by hematoxylin and eosin (H&E) staining. As shown in Fig. 4, the tumor tissues from the PDT group were sparser compared with the other groups, which further verified the efficacy of PDT. Meanwhile, there were no significant differences in the histological patterns of the heart, liver, spleen, lung and kidney in any group, suggesting that the UCNP@TBD nanocomposite has no significant *in vivo* toxicity.

4. Conclusions

In summary, we designed and synthesized a new NIR light excitable UCNP@TBD nanocomposite for photodynamic anticancer therapy. The elaborate design of the spectral overlap and physical distance between AIE PS and UCNP enabled the UCNP@TBD nanocomposite to efficiently generate cytotoxic ROS when excited by NIR light. Due to the remarkable advantages, including efficient ROS generation under NIR light excitation, superior photostability and biocompatibility, the developed NIR light excited PDT offers efficient *in vitro* cancer cell ablation and *in vivo* tumor growth inhibition performance, breaking the contradiction between penetration depth and excitation volume existing in conventional PDT. This study highlights the great potential in developing NIR light excitable nanocomposites for future translational research.

Conflicts of interest

There are no conflicts to declare.

Acknowledgements

S. D., W. W., and T. P. contributed equally to this work. This work was supported by the Natural Science Foundation of China (61805135 and 11974123), Pujiang Talents Program (18PJ1405100), the National Key Research and Development Program of China (2019YFC1604604), Science and Technology Program of Guangzhou (2019050001), Shanghai Jiao Tong University (ZH2018QNA43), Open Project Program of Wuhan National Laboratory for Optoelectronics (2019WNLOKF019).

Notes and references

1 L. Cheng, C. Wang, L. Feng, K. Yang and Z. Liu, *Chem. Rev.*, 2014, **114**, 10869–10939.
2 X. Li, J. F. Lovell, J. Yoon and X. Chen, *Nat. Rev. Clin. Oncol.*, 2020, **17**, 657–674.
3 F. Xiao, B. Cao, L. Wen, Y. Su, M. Zhan, L. Lu and X. Hu, *Chin. Chem. Lett.*, 2020, **31**, 2516–2519.
4 J. Meulemans, P. Delaere and V. Vander Poorten, *Curr. Opin.*, 2019, **27**, 136–141.
5 M. G. Mokwena, C. A. Kruger, M. T. Ivan and A. Heidi, *Photodiagn. Photodyn. Ther.*, 2018, **22**, 147–154.
6 A. Kawczyk-Krupka, A. M. Bugaj, W. Latos, K. Zaremba, K. Wawrzyniec and A. Sieron, *Photodiagn. Photodyn. Ther.*, 2015, **12**, 545–553.
7 D. Dejg, D. Fukumura, R. K. Jain, D. Dejg, D. Fukumura and R. K. Jain, *Nat. Rev. Cancer*, 2003, **3**, 380–387.
8 M. M. Islam, Z. Hu, Q. S. Wang, C. Redshaw and X. Feng, *Mater. Chem. Front.*, 2019, **3**, 762–781.
9 Y. Yuan, G. Feng, W. Qin, B. Z. Tang and B. Liu, *Chem. Commun.*, 2014, **50**, 8757–8760.
10 J. Mei, N. L. C. Leung, R. T. K. Kwok, J. W. Y. Lam and B. Z. Tang, *Chem. Rev.*, 2015, **115**, 11718–11940.
11 B. Gu, K. T. Yong and B. Liu, *Small Methods*, 2018, **2**, 1700392.
12 S. Xu, Y. Yuan, X. Cai, C.-J. Zhang, F. Hu, J. Liang, G. Zhang, D. Zhang and B. Liu, *Chem. Sci.*, 2015, **6**, 5824–5830.
13 J. C. Ge, M. H. Lan, B. J. Zhou, W. M. Liu, L. Guo, H. Wang, Q. Y. Jia, G. L. Niu, X. Huang, H. Y. Zhou, X. M. Meng, P. F. Wang, C. Lee, W. J. Zhang and X. D. Han, *Nat. Commun.*, 2014, **5**, 4596.
14 J. Liu, P. Du, H. Mao, L. Zhang, H. Ju and J. Lei, *Biomaterials*, 2018, **172**, 83–91.
15 W. Pang, P. F. Jiang, S. H. Ding, Z. Z. Bao, N. T. Wang, H. X. Wang, J. L. Qu, D. Wang, B. Gu and X. B. Wei, *Adv. Healthcare Mater.*, 2020, **9**, 2000607.
16 D. Zhang, L. Wen, R. Huang, H. Wang, X. Hu and D. Xing, *Biomaterials*, 2018, **153**, 14–26.
17 Z. Wang, M. Zhan, W. Li, C. Chu, D. Xing, S. Lu and X. Hu, *Angew. Chem., Int. Ed.*, 2021, **60**, 4720–4731.
18 Y. Y. Liu, X. F. Meng and W. B. Bu, *Coord. Chem. Rev.*, 2019, **379**, 82–98.
19 K. R. Deng, C. X. Li, S. S. Huang, B. G. Xing, D. Y. Jin, Q. G. Zeng, Z. Y. Hou and J. Lin, *Small*, 2017, **13**, 1702299.
20 T. Yang, L. Liu, Y. Deng, Z. Guo, G. Zhang, Z. Ge, H. Ke and H. Chen, *Adv. Mater.*, 2017, **29**, 1700487.

21 Z. He, L. Zhao, Q. Zhang, M. Chang, C. Li, H. Zhang, Y. Lu and Y. Chen, *Adv. Funct. Mater.*, 2020, **30**, 1910301.
22 B. Gu, C. Zhao, A. Baev, K. T. Yong, S. Wen and P. N. Prasad, *Adv. Opt. Photonics*, 2016, **8**, 328.
23 B. Gu, W. B. Wu, G. X. Xu, G. X. Feng, F. Yin, P. H. J. Chong, J. L. Qu, K. T. Yong and B. Liu, *Adv. Mater.*, 2017, **29**, 1701076.
24 Q. N. Lin, Q. Huang, C. Y. Li, C. Y. Bao, Z. Z. Liu, F. Y. Li and L. Y. Zhu, *J. Am. Chem. Soc.*, 2010, **132**, 10645–10647.
25 Z. Zheng, H. Liu, S. Zhai, H. Zhang, G. Shan, R. T. Kwok, C. Ma, H. H. Sung, I. D. Williams and J. W. Lam, *Chem. Sci.*, 2020, **11**, 2494–2503.
26 K. Ogawa and Y. Kobuke, *Anti-Cancer Agents Med. Chem.*, 2008, **8**, 269–279.
27 B. Gu, A. Pliss, A. N. Kuzmin, A. Baev, T. Y. Ohulchanskyy, J. Damasco, K. T. Yong, S. Wen and P. N. Prasad, *Biomaterials*, 2016, **104**, 78–86.
28 A. V. Kachynski, A. Pliss, A. N. Kuzmin, T. Y. Ohulchanskyy, A. Baev, J. Qu and P. N. Prasad, *Nat. Photonics*, 2014, **8**, 455–461.
29 M. Wang, J. Song, F. F. Zhou, A. R. Hoover, C. Murray, B. Q. Zhou, L. Wang, J. L. Qu and W. R. Chen, *Adv. Sci.*, 2019, **6**, 1802157.
30 Q. Zhan, H. Liu, B. Wang, Q. Wu, R. Pu, C. Zhou, B. Huang, X. Peng, H. Ågren and S. He, *Nat. Commun.*, 2017, **8**, 1058.
31 M. R. Hamblin, *Dalton Trans.*, 2018, **47**, 8571–8580.
32 N. M. Idris, M. K. Gnanasammandhan, J. Zhang, P. C. Ho, R. Mahendran and Y. Zhang, *Nat. Med.*, 2012, **18**, 1580–1585.
33 L. M. Maestro, E. M. Rodriguez, F. Vetrone, R. Naccache, H. L. Ramirez, D. Jaque, J. A. Capobianco and J. G. Solé, *Opt. Express*, 2010, **18**, 23544–23553.
34 C. Wang, L. Cheng, Y. M. Liu, X. J. Wang and X. X. Ma, *Adv. Funct. Mater.*, 2013, **23**, 3077–3086.
35 M. Yang, H. Wang, Z. Wang, Z. Han and Y. Gu, *Biomater. Sci.*, 2019, **7**, 1686–1695.
36 Z. X. Zhao, Y. N. Han, C. H. Lin, D. Hu and F. Wang, *Chem.–Asian J.*, 2012, **7**, 830–837.
37 H. S. Qian, H. C. Guo, C. L. Ho, R. Mahendran and Y. Zhang, *Small*, 2010, **5**, 2285–2290.
38 Y. Guan, H. G. Lu, W. Li, Y. D. Zheng and H. Gao, *ACS Appl. Mater. Interfaces*, 2017, **9**, 26731–26739.
39 G. Jin, R. He, Q. Liu, M. Lin, Y. Dong, K. Li, B. Z. Tang, B. Liu and F. Xu, *Theranostics*, 2019, **9**, 246–264.
40 J. M. Li, C. W. T. Leung, D. S. H. Wong, J. B. Xu and R. Li, *ACS Appl. Mater. Interfaces*, 2017, **11**, 22074–22084.
41 D. Mao, F. Hu, Z. Yi, K. Kenry, S. Xu, S. Yan, Z. Luo, W. Wu, Z. Wang and D. Kong, *Sci. Adv.*, 2020, **6**, eabb2712.
42 X. H. Zhu, J. Zhang, J. L. Liu and Y. Zhang, *Adv. Sci.*, 2019, **6**, 1901358.
43 Q. Zhan, J. Qian, H. Liang, G. Somesfalean and S. Andersson-Engels, *ACS Nano*, 2011, **5**, 3744–3757.
44 S. Shi, X. Zhu, Z. Zhao, W. Fang, M. Chen, Y. Huang and X. Chen, *J. Mater. Chem. B*, 2013, **1**, 1133–1141.
45 B. Tian, C. Wang, S. Zhang, L. Feng and Z. Liu, *ACS Nano*, 2011, **5**, 7000–7009.
46 S. He, N. J. J. Johnson and V. A. N. Huu, *Chem. Mater.*, 2018, **30**, 3991–4000.
47 W. Wu, D. Mao, S. Xu, S. Ji, F. Hu, D. Ding, D. Kong and B. Liu, *Mater. Horiz.*, 2017, **4**, 1110–1114.
48 F. Wang, R. Deng and X. Liu, *Nat. Protoc.*, 2014, **9**, 1634–1644.
49 K. Li and B. Liu, *J. Mater. Chem.*, 2011, **22**, 1257–1264.
50 D. Wang, B. Xue, X. Kong, L. Tu, X. Liu, Y. Zhang, Y. Chang, Y. Luo, H. Zhao and H. Zhang, *Nanoscale*, 2014, **7**, 190–197.
51 F. Ai, Q. Ju, X. Zhang, X. Chen, F. Wang and G. Zhu, *Sci. Rep.*, 2015, **5**, 10785.
52 Y. Zhao, Q. Zhan, J. Liu and S. He, *Biomed. Opt. Express*, 2015, **6**, 838–848.
53 C. J. Zhang, Q. L. Hu, G. X. Feng, R. Y. Zhang, Y. Y. Yuan, X. M. Lu and B. Liu, *Chem. Sci.*, 2015, **6**, 4580–4586.
54 D. Jaque, L. M. Maestro, B. D. Rosal, P. Haro-Gonzalez, A. Benayas, J. L. Plaza, E. M. Rodríguez and J. G. Solé, *Nanoscale*, 2014, **6**, 9494–9530.